JACS
JOURNAL OF THE AMERICAN CHEMICAL SOCIETY

Article

pubs.acs.org/JACS

Atomically Precise Doping of Monomanganese Ion into Coreless Supertetrahedral Chalcogenide Nanocluster Inducing Unusual Red Shift in Mn^{2+} Emission

Jian Lin,[†] Qian Zhang,[†] Le Wang,[†] Xiaochun Liu,[†] Wenbo Yan,[†] Tao Wu,*[,†] Xianhui Bu,*[,‡] and Pingyun Feng*[,§]

[†]College of Chemistry, Chemical Engineering and Materials Science, Soochow University, Jiangsu 215123, China

[‡]Department of Chemistry and Biochemistry, California State University, 1250 Bellflower Blvd., Long Beach, California 90840, United States

[§]Department of Chemistry, University of California, Riverside, California 92521, United States

Supporting Information

ABSTRACT: We report a simple and yet effective method to introduce Mn^{2+} ions into semiconducting nanoclusters with atomically precise control. Our method utilizes one type of micrometer-sized crystals, composed of well-defined isolated supertetrahedral chalcogenide nanoclusters (~2 nm, $[Cd_6In_{28}S_{52}(SH)_4]$) whose core metal site is unoccupied in as-synthesized pristine form. This unique model structure with vacant core site makes it possible to achieve ordered distribution of Mn^{2+} dopants, and at the same time effectively preclude the formation of Mn^{2+} clusters in the host matrix. A two-step synthesis strategy is applied to realize an atomically precise doping of Mn^{2+} ion into the core site of the nanoclusters, and to achieve uniform distribution of Mn^{2+} dopants in the crystal lattice. The PL, X-ray photoelectron (XPS), as well as the electron paramagnetic resonance (EPR) spectra reveal the successful incorporation of Mn^{2+} ion into the core site of the nanocluster. Different from the pristine host material with weak green emission (~490 nm), the Mn^{2+}-doped material shows a strong red emission (630 nm at room temperature and 654 nm at 30 K), which is significantly red-shifted relative to the orange emission (~585 nm) observed in traditional Mn^{2+}-doped II–VI semiconductors. Various experiments including extensive synthetic variations and PL dynamics have been performed to probe the mechanistic aspects of synthesis process and resultant unusual structural and PL properties. The quaternary semiconductor material reported here extends the emission window of Mn^{2+}-doped II–VI semiconductor from yellow-orange to red, opening up new opportunities in applications involving photonic devices and bioimaging.

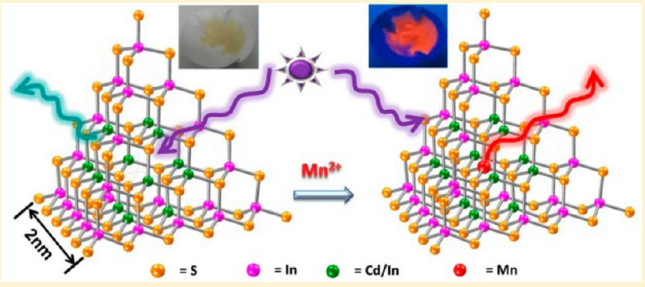

INTRODUCTION

Metal chalcogenides and nanoclusters are among the most advanced solid-state materials because of their many applications.[1−13] In addition to the direct synthesis, doping and postsynthetic modification of host materials to generate desirable functions are a powerful synthetic strategy in new materials design, as well as an established technological process to control and manipulate optical, electronic, and catalytic properties of solid materials[14−24] and molecular-based materials.[25−29] Among a variety of host materials, II–VI semiconductors (such as ZnS, CdS, ZnSe, CdSe) have attracted significant attention because new properties originating from the dopants can be created through the interaction of dopants with charge carriers in the semiconductor host frameworks.[30,31] The early study on semiconductor doping focused on the bulk ones. With the development of nanomaterials in recent several decades, considerable efforts have been devoted to doping semiconductor nanocrystals (NCs) or quantum dots (QDs).[14,23,32,33] It is mainly because the dopants can create intermediate electronic states, while retaining intrinsic advantages of NCs, through stronger interaction of dopants with charge carriers in the spatially confined host NCs than that in bulk counterparts.[34] Dopants can further change photophysical relaxation process by altering the charge separation and recombination dynamics, which are related to the creation of new optical, photochemical, electronic, and photoexcited relaxation properties.[35]

In addition to composition and size of host materials, the type of dopants also plays a vital role in tuning the optical and electronic properties of semiconductors. Doping behaviors by transition metal ions in chalcogenide NCs are of particular interest owing to the fact that the transition metal ligand-field excited states usually reside within the band gap of the host semiconductors.[36,37] In particular, Mn^{2+} ion has proved to be perfect impurity serving as trap state in II–VI semiconductor

Received: February 6, 2014
Published: March 13, 2014

   dx.doi.org/10.1021/ja501288x | J. Am. Chem. Soc. 2014, 136, 4769−4779

NCs for the following reasons:[38] (i) Mn^{2+} ion with the $3d^5$ acting as a half-filled shell is more likely to resemble group IIB elements (such as the Zn and Cd with d^{10} shell) in its behavior than other transition metal elements; (ii) paramagnetic Mn^{2+} ions ($S = 5/2$) can convert nonmagnetic parent semiconductors into intriguing magnetic materials, called diluted magnetic semiconductors (DMSs), because of the coupling of the localized magnetic moments of Mn^{2+} ions with the band electrons through the exchange interaction;[39−41] and (iii) Mn^{2+} ion, acting as recombination center for the excited electron−hole pairs, exhibits a strong and typical photoluminescence (PL) emission centered at a wavelength of ∼585 nm (∼2.12 eV) originating from the $^4T_1(G) \rightarrow {}^6A_1(S)$ transition in 3d shell of the tetrahedrally coordinated Mn^{2+} ions. Notably, such special PL property is not observed in Mn^{2+}-containing or Mn^{2+}-doped polyoxometalate.[42−44] Since the Mn^{2+}-doped ZnS semiconductor nanoparticles with intriguing PL property was first reported almost 20 years ago,[38] the Mn^{2+}-doped semiconductor materials with high emission efficiency and excellent chemical stability have been at the heart of many technologies, such as luminescence sensors,[45] LEDs,[46] photovoltaic cells,[47−49] spintronics,[50] and bioimaging.[51−53] Although these Mn^{2+}-doped semiconductor emitters have been well developed through various synthetic strategies, there are still some limitations. For instance, most Mn^{2+}-involved doping processes occur in the II−VI system, and few cases on III−V,[54] I−III−VI,[55,56] or II−III−VI semiconductors are reported; Mn^{2+}-related emission wavelength is also confined in the range of 580−600 nm, and only few examples with longer emission wavelength have been reported.[57−59] For these reasons, efforts are needed to pursue larger ensemble Stokes shifts in Mn^{2+}-doped chalcogenides, which could further reduce the self-absorption effects and are desirable in the light-emitting and bioimaging applications.[60,61]

Moreover, the degree of homogeneity of Mn^{2+} ions in the host lattice is essential for achieving efficient luminescence and tailoring the emission position.[19,62] Some synthetic strategies and methods have been developed to seek the elaborate control of the distribution of dopants in bulk and NC semiconductor host lattices. Still, for bulk semiconductors with dense phase, it is difficult to achieve large doping level and the ordered dopant distribution at the same time, and only a small fraction of the initially added Mn^{2+} ions is incorporated into the crystal lattice, while a large portion of them remain on the surface (Scheme 1a). When the bulk crystals are shrunk down to NCs, a higher degree of doping level can be achieved (Scheme 1b). So far, the use of the "decoupling doping from nucleation and/or growth" concept has made it possible to dope most NCs with controlled radial distribution of the dopants,[63−65] but the radial location of dopants in the NCs was either random or poorly controlled, and there are still big challenges in controlling the ordered and uniform distribution of dopants through the whole lattice in NCs. Furthermore, most doping processes readily change the size uniformity of NCs. Therefore, how to realize the high degree of homogeneity of Mn^{2+} ions in the whole crystal lattice while avoiding the formation of irregular Mn^{2+}-cluster is an interesting and challenging topic facing materials scientists. Further research also requires development of new synthetic technique to realize the uniform distribution of dopants in either bulky or NCs semiconductors in desirable and controllable ways.

Recently, we reported a micrometer-sized crystal (denoted as ISC-10-CdInS) composed of isolated coreless supertetrahedral

Scheme 1. Distribution of Dopants in Three Different Crystal Models[a]

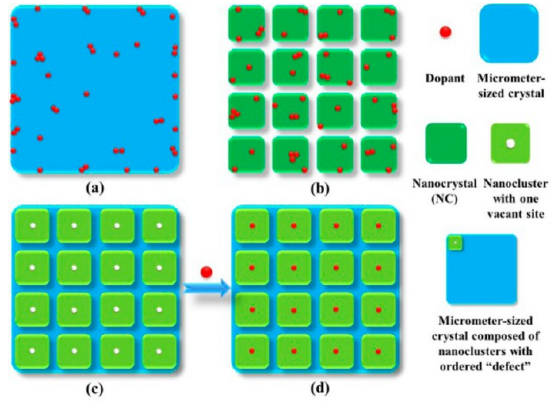

[a](a) Bulk crystal with dense phase, (b) nanocrystals with dense phase, and (c) micrometer-sized crystal composed of nanoclusters with the ordered "intrinsic internal defects". (d) An ideal doping mode with a uniform distribution of dopants in the whole crystal lattice, which is obtained through post-synthetic modification (this work).

chalcogenide nanoclusters ($[Cd_6In_{28}S_{52}(SH)_4]$) with the dimension of ∼2 nm in edge length.[66] This material exhibits semiconducting characteristics with tunable photoelectric response behavior. Such isolated nanocluster can be treated as discrete QD separated from each other with ∼1.5 nm intercluster distance by charge-balancing organic species, analogous to the protective organic ligand in NCs. An unusual feature of this cluster is that there is a well-defined vacant site at the core of supertetrahedral nanocluster (denoted as T5-CdInS, "T" means tetrahedral, "5" is the number of metal layers in the cluster followed by the composition of cluster) with 34 metal sites (6 Cd^{2+} ions and 28 In^{3+} ions). It can thus be regarded as a "○@CdS@InS core-shell" nanostructure (○ means vacant position). Such vacant position in the nanocluster can be viewed as ideal "defect". The micrometer-sized crystal containing isolated naonocluters exhibits ordered distribution of "intrinsic internal defects (IID)" throughout the whole crystal lattice (Scheme 1c). Interestingly, the vacancies have proved to trap Cu^+ ions through a facile diffusion process at relatively low temperature, as confirmed by single-crystal X-ray diffraction technique. Inspired by this result, we hypothesized that this unique nanocluster could be a perfect model for the study on the Mn^{2+}-doped emitters. Although there is a distinct difference in bond energy between Mn−S (301 kJ/mol) and Cu−S (274.5 kJ/mol), similar ionic radii (0.80 Å for Mn^{2+}, 0.75 Å for Cu^+) and the higher positive charge could facilitate the trapping of one Mn^{2+} ion at the core site. Compared with both pure micrometer-sized bulk semiconductor with dense phase and NCs, this host model shows several potential advantages for enhancing Mn^{2+}-doped emitters: (i) the unique core−shell nanostructure with well-defined cationic vacancy facilitates the control of the precise doping by avoiding the formation of Mn-pairs in the nanocluster; (ii) the uniform size of nanocluster can exclude the interference of size nonuniformity on PL peak emission, making it possible to just consider the effect of sulfide ligands surrounding dopants; (iii) this II−III−VI semiconductor serves as a totally new host lattice for Mn^{2+} doping, which could alter Mn^{2+}-related emission energy.

Herein, we applied a two-step synthetic strategy to purposefully introduce a single manganese ion into coreless

dx.doi.org/10.1021/ja501288x | J. Am. Chem. Soc. 2014, 136, 4769−4779

supertetrahedral nanoclusters. A detailed investigation on PL and EPR of Mn^{2+}-doped ISC-10-CdInS sample confirmed the presence of Mn^{2+} ion and its location. This synthetic strategy is very effective in controlling the doping level and in achieving uniform distribution of Mn^{2+} ions. In contrast with weak green emission (~490 nm) and short lifetime (approximate hundreds of nanoseconds) of pristine materials, the Mn^{2+}-doped sample shows a strong red emission (630 nm at room temperature and 654 nm at 30 K), which is a dramatic red shift relative to the orange emission (~585 nm) observed in typical Mn^{2+}-doped II–VI semiconductors. This red emission with long decay lifetime (~1.1 ms) is ascribed to the energy-narrowed $^4T_1 \rightarrow {}^6A_1$ transition in 3d shell of Mn^{2+} ion,[67,68] which results from of the "crystal lattice strain" induced by the special supertetrahedral "Mn@CdS@InS core-shell" nanostructure with T_d symmetry. To our knowledge, this is the first study on the PL properties of the Mn^{2+}-doped microcrystal composed of supertetrahedral chalcogenide nanoclusters.

EXPERIMENTAL SECTION

Chemicals. Cadmium nitrate tetrahydrate ($Cd(NO_3)_2{\cdot}4H_2O$, AR, 99%), zinc nitrate hexahydrate ($Zn(NO_3)_2{\cdot}6H_2O$, AR, 99%), indium powder (In, 99.99%, 200 mesh), sulfur powder (S, 99.99% metals basis), manganese(II) acetate tetrahydrate ($Mn(Ac)_2{\cdot}4H_2O$, 99.99% metals basis), piperidine (PR, 99%), and 1,5-diazabicyclo[4.3.0]non-5-ene (DBN, 98%) were purchased from Aladdin Industrial, Inc. All chemicals were used as received without further purification.

Syntheses. The microcrystals of ISC-10-CdInS ($[Cd_6In_{28}S_{52}(SH)_4]{\cdot}[H^+\text{-DBN}]_8{\cdot}[H^+\text{-PR}]_4$) were synthesized following literature method.[66] Its zinc analogue (coded as ISC-10-ZnInS) was prepared through a similar method, by replacing cadmium salt with zinc salt. Mn^{2+}-doped samples were prepared by adding different concentrations of $Mn(Ac)_2$ aqueous solution into a 23 mL Teflon reaction vessel containing 2.0 g of mixed solvents (DBN and PR with the mass ratio of 1:1) and undoped sample of 30.0 mg, which was then sealed in stainless steel autoclave and heated at 150 °C for 5 days. The autoclave was subsequently cooled to the room temperature. The resulting products were taken out of autoclave, and washed with ethanol three times and deionized (DI) water twice. Finally, pale-yellow octahedral crystals were obtained with the yield close to 100% after drying in air. To ensure the complete removal of the unreacted Mn^{2+} ions or other unknown Mn^{2+}-containing species adsorbed on the surface of microcrystals, doped samples were washed thoroughly with dilute HCl acid solution (pH ~ 2.5).[69]

Physical Characterization. Powder X-ray diffraction (XRD) measurements were carried out with a diffractometer (X'Pert-Pro MPD, PANalytical, Holland) using Cu Kα (λ = 1.54056 Å) radiation. Solid-state diffuse reflectance spectra were recorded on a SHIMADZU UV-3600 UV–vis–NIR spectrophotometer. The absorption spectra were calculated from reflectance spectra by using the Kubelka–Munk function: $F(R) = \alpha/S = (1 - R)^2/2R$, where R, α, and S are the reflection, the absorption, and the scattering coefficient, respectively. In order to determine the band edge of the direct-gap semiconductor, the relation between the absorption coefficients (α) and the incident photon energy ($h\nu$) is exhibited as $\alpha h\nu = A(h\nu - E_g)^{1/2}$, where A is a constant that relates to the effective masses associated with the valence and conduction bands, and E_g is the optical transition gap of the solid material. By extrapolating the linear region to the abscissa, the band gap E_g can be estimated.[70] PL and photoluminescence excitation (PLE) spectra were recorded by an Edinburgh FLS920 steady state and time-resolved fluorescence spectrophotometer equipped with a 450 W xenon lamp. In each measurement, the same amount of sample was used. PL decays were recorded using an Edinburgh FLS920 steady state fluorimeter with a time-correlated single-photon counting (TCSPC) spectrometer and a pulsed xenon lamp as the excitation source. PL quantum-yield (PLQY) was recorded using a Horiba Jobin Yvon Fluoromax-4 with a quantum-yield accessory. Electron paramagnetic resonance (EPR) measurements were carried out on powder samples at 9.06 GHz using an ER200-SRC Bruker X-band spectrometer at room temperature. X-ray photoelectron spectroscopy (XPS) data were collected with a Leeman prodigy spectrometer equipped with a monochromatic Al Kα X-ray source and a concentric hemispherical analyzer. The actual Mn^{2+} doping levels were determined by inductively coupled plasma-atomic emission spectrometry (ICP-AES).

RESULTS AND DISCUSSION

Doping Process and Structure Characterization. The model compound (ISC-10-CdInS) was synthesized through solvothermal reaction following previous procedure.[66] A 10-min ultrasonic washing step was carried out to remove undetectable impurities and small powdery crystals, and only pure micrometer-sized crystals were collected for the following experiments. The Mn^{2+}-doping process was carried out by directly mixing manganese salts with raw host materials via ion diffusion (Figure 1a). To prevent possible damage of nanoclusters from overheating, the diffusion process was controlled at a relatively low temperature (150 °C). Notably, among the doping approaches designed to control the dopant distribution, the present doping protocol using micrometer-sized crystals with the "intrinsic internal defects" was much more convenient than the previously reported doping processes, such as nucleation-doping and growth-doping for the creation of semiconductor NCs.[63−65]

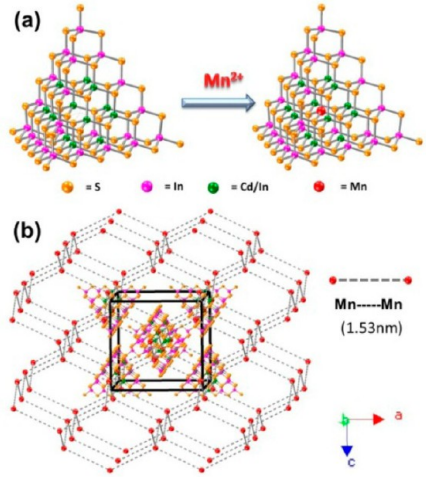

Figure 1. (a) The schematic graph of doping process of one Mn^{2+} ion into one coreless supertetrahedral chalcogenide nanocluster. (b) The ideal distribution of Mn^{2+} ions in the crystal lattice with separation distance of 1.53 nm between two adjacent Mn^{2+} ions.

Figure 2a showed the powder X-ray diffraction patterns of as-synthesized and Mn^{2+}-doped ISC-10-CdInS samples. Their similar diffraction patterns suggested that the overall cluster structure and packing mode were retained. Compared with the simulated pattern of the undoped sample, the main peak of Mn^{2+}-doped sample around the 5° split into several peaks, likely due to minor lattice distortion during the incorporation of Mn^{2+} ions into coreless T5 nanoclusters. Similarly, the quality of crystals following the doping became lower so that other methods (instead of single crystal X-ray diffraction) were used here to indicate Mn^{2+} ions being located at the core site of the coreless T5 nanoclutster. In addition, the doping process led to a slight shift of the PXRD peaks to larger angles, which

dx.doi.org/10.1021/ja501288x | J. Am. Chem. Soc. 2014, 136, 4769–4779

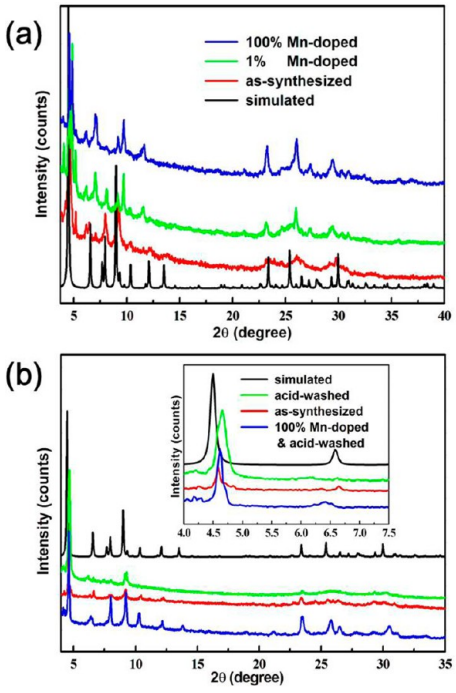

Figure 2. The powder XRD patterns of undoped and Mn^{2+}-doped samples: (a) unwashed, (b) acid-washed. The simulated diffraction pattern is based on the single-crystal structure of the undoped sample.

meant that the unit cell volume of the doped sample became smaller after doping. This slight shrinkage of the crystal lattice could result from the partial loss of positively charged organic template molecules, caused by the introduction of positively charged Mn^{2+} ions, which reduced the negative charge of the nanocluster.

To eliminate the possible interference on the PL measurements from surface-adsorbed Mn^{2+} ions, the raw Mn^{2+}-doped samples were washed with diluted HCl acid. This washing step caused a minor change to the structure of host matrix, as indicated in Figure 2b. The main diffraction peak around the 5° for both undoped-washed and doped-washed sample shifted to the higher angle. On the basis of the lower C/H/N content in the washed sample, it is suggested that the peak shift may be caused by partial protonation for sulfide ions on the surface of nanoclusters, which resulted in the partial loss of positively charged organic template molecules and further induces the shrinking of the unit cell.

The Mn^{2+}-doping process reported here was distinctly different from, and more challenging than, the Cu^{+}-doping process. One reason is that the Cu^{+} ion has stronger affinity for S^{2-} so that it can strip the corner sulfide out of nanocluster to accelerate the dissolution process of T5 nanocluster into the reactant solution and facilitate the diffusion of Cu^{+} ion into the core sites. As observed, addition of extra copper ions could destroy the nanocluster. From the structural viewpoint, the Mn^{2+} ion (0.80 Å) has an ionic radius comparable to that of Cu^{+} ion (0.75 Å), which permits the diffusion of Mn^{2+} into coreless nanocluster to form T5-MnCdInS cluster. Yet, different from Cu^{+}, the addition of extra Mn^{2+} ions would not lead to the collapse of the structure of host materials, which is believed to be due to relatively weaker interaction between Mn^{2+} and S^{2-}. Furthermore, longer reaction time (generally 5 days for Mn^{2+}-doping and 2 days for Cu^{+}-doping) is needed for Mn^{2+}-doping to realize the desired doping pattern when all coreless T5 clusters in the whole crystal lattice encapsulate Mn^{2+} ion at their core sites, as shown in Figure 1b.

To properly label doped samples with different dopant concentration, we define the doping level of Mn^{2+} ions as N%, with N being the moles of Mn^{2+} ions per 100 mols of T5 nanoclusters, which clearly exhibits the doping level of Mn^{2+} ions relative to the theoretically targeted coreless site in nanocluster. Naturally, the value of N for the nominal doping level represents the added number of moles of Mn^{2+}. All doped samples appearing in the text and figures are labeled by this nominal number. The actual concentration of Mn^{2+} ion in doped sample is measured from the ICP-AES analysis, as summarized in Table S1 (Supporting Information). The results show that the measured molar ratios of Mn:In are smaller than their corresponding ideal values at low doping levels, and even smaller than the ideal maximum value of 1:28 (based on the 100% doping level) when excessive dopant concentrations are applied. These results suggest that not all coreless nanoclusters are involved in the doping process, and importantly, they suggest that the incorporated Mn^{2+} results from the diffusion of Mn^{2+} into the empty core sites of the cluster, instead of through ion exchange with Cd^{2+} ions.

The presence of In, Cd, Mn, and S in the acid-treated sample with nominal 10% Mn^{2+} doping level (corresponding to 3.1% in the actual number) was also confirmed by X-ray photoelectron spectroscopy (XPS). As shown in Figure 3, the peaks

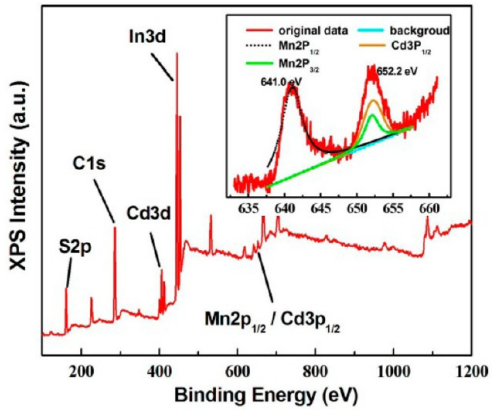

Figure 3. XPS of acid-washed sample with nominal 10% Mn^{2+}-doping level. Inset is Mn 2p spectrum with deconvolution, revealing the overlap of Cd $3p_{1/2}$ and Mn $2p_{1/2}$ peaks.

of S2p, Cd3d and In3d appear at 161.5, 404.6, and 444.2 eV respectively. The peak around at 653 eV is the result of overlap between Cd $3p_{1/2}$ peak and Mn $2p_{1/2}$ peak, which is clearly shown in the deconvoluted peak of Mn 2p (Mn $2p_{3/2}$ at 641.1 eV and Mn $2p_{1/2}$ at 652.2 eV).[71]

Absorption Spectrum and Optical Band Gap. The adsorption spectra of unwashed and washed samples of ISC-10-CdInS derived from the diffuse reflectance spectrum through Kubelka–Munk function ($F(R) = (1 - R)^2/2R$) are shown in Figure 4a. The absorption edge of acid-washed sample is shifted to lower energy compared with that of unwashed raw sample, which could be attributed to the slight change on surface structure of nanocluster, as discussed above. For the semiconductor with allowed direct transition, the corresponding band gap (E_g) was usually obtained though extrapolating the linear portion of plot of $(\alpha h\nu)^2$ vs $h\nu$ to $\alpha = 0$ value.[72] On the basis of this method, the optical band gap of raw sample, as

dx.doi.org/10.1021/ja501288x | J. Am. Chem. Soc. 2014, 136, 4769–4779

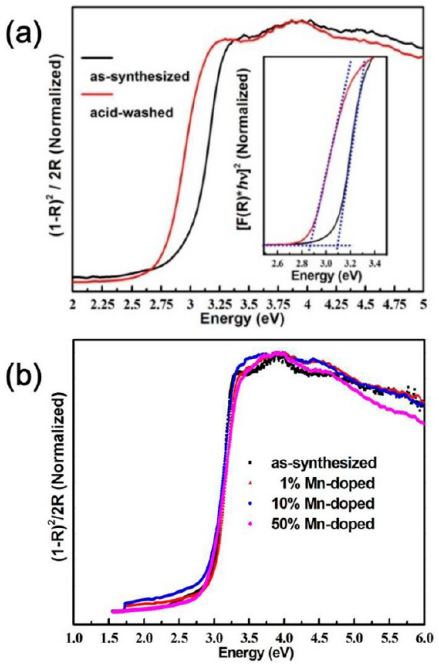

Figure 4. Adsorption spectra of solid sample from the diffuse reflectance spectra through KM function: (a) raw and acid-washed ISC-10-CdInS, and inset is plot of $(\alpha h\nu)^2$ vs $h\nu$; (b) Mn^{2+}-doped sample with different nominal doping levels. The spectra were normalized for absorbance at 310 nm (3.8 eV).

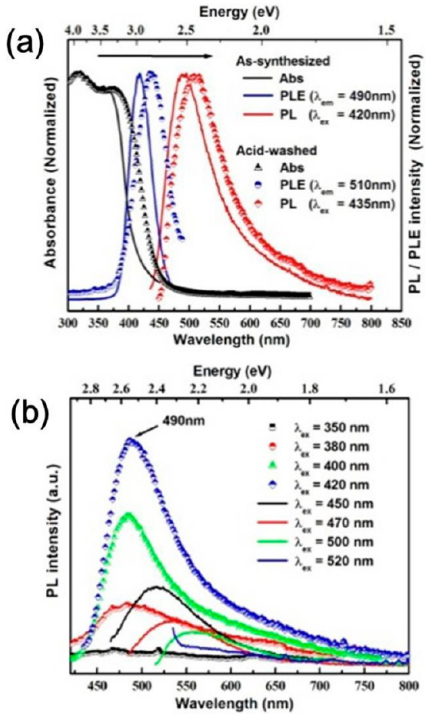

Figure 5. (a) Adsorption, photoluminescence (PL) and photoluminescence excitation (PLE) spectra of raw host material and acid-treated sample at room temperature. (b) PL spectra of raw sample under different excitation wavelength ranging from 350 to 520 nm.

shown in the inset of Figure 4a, was calculated to be 3.10 eV, much higher than that of bulk sample $CdIn_2S_4$ (2.3 eV),[73] bulk CdS (2.5 eV), and β-In_2S_3 (2.1 eV), which could be partially attributed to the quantum confinement effect. The band gap of acid-washed sample also displays a red shift to 2.87 eV, consistent with the absorption change. It is worth noting that the band gap of Mn^{2+}-doped sample with various doping levels is very close to that of undoped sample (Figure 4b), which is much greater than that of Cu^+-doped sample (E_g = ~2.11 eV). The minor impact of Mn^{2+} ion on the band gap of host material is due to the localized nature of the transition within the $3d^5$ configuration of Mn^{2+}.

Photoluminescence Properties. The PL and photoluminescence excitation (PLE) spectra of raw host material are displayed in Figure 5a. The PLE spectrum monitored at 490 nm has the narrow and symmetric shape centered at 420 nm. However, a broad and asymmetric spectrum peaked at 490 nm is observed when excited at 420 nm. Figure 5b shows excitation-wavelength dependent PL spectra. As observed, the peak position remains unchanged and only emission intensity increases with the increasing excitation wavelength (<420 nm). However, it becomes weaker and gradually shifts to longer wavelength with the increasing excitation wavelength (>420 nm). This trend, together with the broad and asymmetric spectral shape, indicates a possible complicated PL mechanism involving multiple recombination pathways of photoexcited electrons and holes. Clearly, large Stokes shift between the absorption onset and the PL peak suggests that band emission is suppressed, and the dominant green emission is likely from a radiative recombination of charge carriers at trap states or defect centers, i.e., surface states and intrinsic states.[74]

The PL properties of the acid-treated sample are also investigated. As shown in Figure 5a, the maximum excitation wavelength for washed sample is red-shifted to 435 nm compared with unwashed sample. Correspondingly, the maximum PL emission peak is red-shifted to 510 nm while keeping the broad spectral shape. We notice that the maximum excitation energy (2.85 eV) is in agreement with the band gap of acid-washed sample (2.87 eV). Thus, the red shift for both optical absorption and emission band may be ascribed to the gap change of T5 structure caused by acid-washing.

The PLE and PL spectra of Mn^{2+}-doped sample are also investigated. When 1% Mn^{2+}-doped sample is excited at the wavelength of 400 nm, two emission bands are observed, as shown in Figure 6a. One is a weak green emission band located at 490 nm, and the other is the dominant red emission band with Gaussian shape peaked at 630 nm. Obviously, the green peak is assigned to the emission from host materials, and the emerging red emission must be related to the Mn^{2+}dopants. We further study excitation-wavelength dependent PL property of 1% Mn^{2+}-doped sample by systematically changing excitation wavelength from 300 nm to 450 nm. As displayed in Figure 6b, with an increase of λ_{ex} from 300 nm from 400 nm, the emission intensity of both emission bands, with the I_g/I_r ratio less than 1, becomes stronger. However, when excited at 420 nm, the I_g/I_r ratio becomes greater than 1, and the red emission peak even disappears when excited at 450 nm.

Figure 7 shows the relationship between the intensity/position of the dominant red emission and Mn^{2+}-doping level. With the increasing Mn^{2+} content, the intensity of red emission increases, while green emission intensity decreases dramatically. When the nominal Mn^{2+}-doping level reaches to 50%, the host lattice emission (490 nm) is suppressed to the almost undetectable level. As shown in the inset of Figure 7, when excited with 365 nm UV lamp, 50% Mn^{2+}-doped sample exhibits an enhanced red emission with PL quantum yield of

dx.doi.org/10.1021/ja501288x | J. Am. Chem. Soc. 2014, 136, 4769−4779

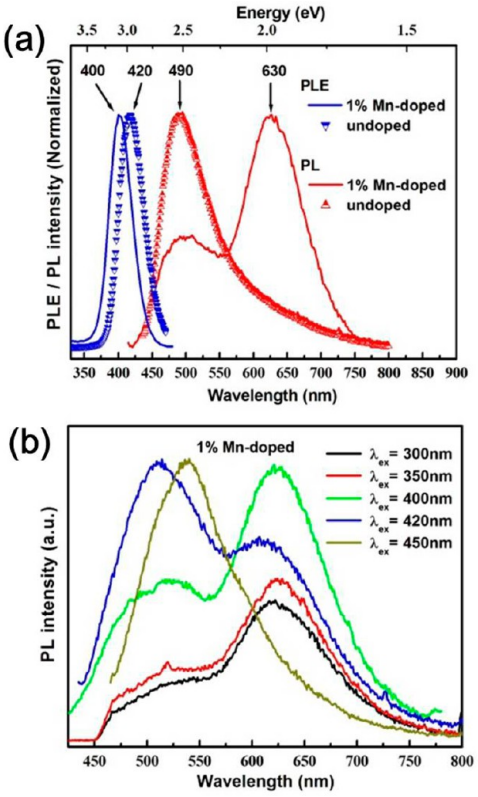

Figure 6. (a) The PLE and PL spectra of 1% Mn^{2+}-doped sample when the emission is monitored at 630 nm. The undoped sample was also shown here for convenient comparison. (b) Excitation-wavelength dependent PL spectra of 1% Mn^{2+}-doped sample at different excitation wavelength ranging from 300 nm to 450 nm.

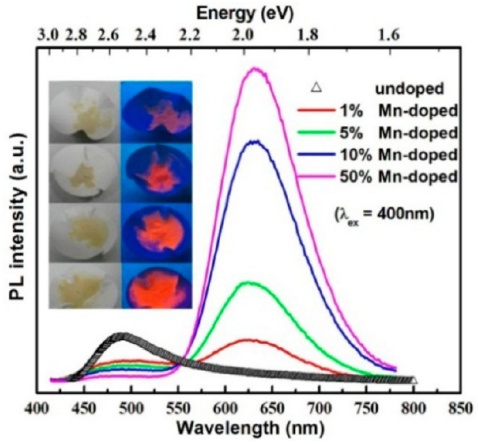

Figure 7. Mn^{2+}-doping level dependent PL spectra. Insert: optical images of solid doped sample with different doping levels under 365 nm UV lamp excitation.

0.53%. Notably, the different Mn^{2+}-doping levels do not change peak position of red emission.

To further confirm that the dominant red emission of Mn^{2+}-doped samples originates from the Mn^{2+} ion in the crystal lattice, rather than one adsorbed on the surface of the microcrystal or unreacted metal salt, two comparative experiments are carried out. In the first experiment, the raw ISC-10-CdInS sample is mechanically mixed with the manganese salt, and for this mixture no red emission peak in the region of 550–650 nm is observed (Figure S1a, Supporting Information). In the second one, UCR-5-ZnInS sample, composed of super-tetrahedral T4 nanocluster ($[Zn_4In_{16}S_{36}]$) without vacant core metal site,[75] is treated in the same way as Mn^{2+}-doped ISC-10-CdInS. After treatment, only intrinsic blue-green emission (~460 nm) from host material is observed (Figure S1b, Supporting Information). These results prove that the intrinsic vacant site in the nanocluster plays an important role in the facile diffusion of Mn^{2+} into the host lattice, and the divalent ions in the original nanocluster are not readily ion-exchanged by Mn^{2+} ions at relatively low temperature.

To eliminate the possible interference of Mn^{2+}-containing species attached to the microcrystal surface on the Mn^{2+}-emission position, we investigate the PL of the acid-washed 50% Mn^{2+}-doped sample. The maximum excitation wavelength is red-shifted to 408 nm compared to unwashed and Mn^{2+}-doped sample (Figure S2, Supporting Information). This red shift trend is consistent with that observed in the acid-washed and undoped sample, being ascribed to the structure-induced gap change. The dependence of excitation wavelength on the emission intensity is also observed for this acid-treated sample (Figure 8). It is notable that, unlike the green emission band,

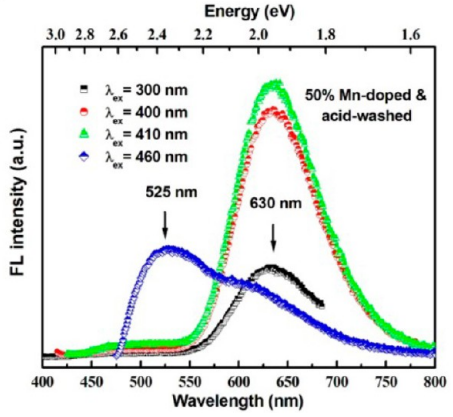

Figure 8. The excitation-wavelength dependent PL spectra of acid-washed 50% Mn^{2+}-doped sample.

the maximum peak for red emission remains at 630 nm and not changed by acid-washing. This further indicates that any small amount of Mn^{2+}-containing species attached to the crystal surface would have little influence on the Mn^{2+}-related emission.

All above PL experiments have unambiguously established that the red emission for Mn^{2+}-doped ISC-10-CdInS is attributed to Mn^{2+} ions in the T5 nanocluster of crystal lattice. It is generally accepted that, for typical Mn^{2+}-doped II–VI semiconductor, Mn^{2+}-related orange emission peak (~585 nm) comes from a rapid energy transfer from the host lattice into the split d-orbital of Mn^{2+} ions and subsequent $^4T_1(^4G) \rightarrow {}^6A_1(^6S)$ transition within the 3d shell of Mn^{2+} ion.[67] In this case, the energy transfer from the photoexcited nanoclusters to the Mn^{2+} ions is also implied due to the fact that excitation spectra of the red emission for Mn^{2+}-doped ISC-10-CdInS is consistent with its absorption onset. However, it should be noted that Mn^{2+}-doped ISC-10-CdInS gives a symmetric red emission centered at 630 nm (1.97 eV) with a large Stokes shift between excitation and emission wavelengths. Why does it have a big red shift?

In principle, the peak wavelength of Mn^{2+} emission depends on crystal field splitting in the host lattice.[50,76] Size-mismatch-

dx.doi.org/10.1021/ja501288x | J. Am. Chem. Soc. 2014, 136, 4769–4779

induced crystal lattice strain observed in one core−shell NCs is ever explained as one factor that leads to a large crystal-field splitting of the Mn^{2+} 3d-orbitals, which correspondingly shrinks $^4T_1 \rightarrow {}^6A_1$ transition energy gap.[77] In this case, when the Mn^{2+} ion is incorporated into the host material, it is perfectly located at the core site of nanocluster with uniform size and T_d symmetry, and correspondingly, the local "crystal lattice strain" is created by the profound mismatch of M−S bond lengths in the "Mn@CdS@InS core-shell" structure, where the Mn−S bond is suppressed in such small void space. Thus, compared to traditional Mn^{2+}-doped CdS crystal lattice, the greater local "crystal lattice strain" occurs in this special nanostructure and causes a greater splitting of Mn^{2+} 3d energy level, which pulls the $^4T_1$ level closer to the $^6A_1$ ground state and consequently induces a big red shift in the Mn^{2+} emission from yellow-orange to red. Moreover, this structure-induced splitting of Mn^{2+} energy level is independent of the charged species surrounding the nanocluster, because no variation in Mn^{2+} emission wavelength is observed for acid-treated sample.

In addition, the exact position of Mn^{2+} $^4T_1 \rightarrow {}^6A_1$ transition can also be affected by the variation in the Mn^{2+} concentration. High Mn^{2+} doping level generally leads to red shift of Mn^{2+} emission due to magnetic interactions between neighboring Mn^{2+} ions.[78,79] However, in this work, with the increasing Mn^{2+}-doping level, the spectral shape and the maximum emission peak (630 nm) stay unchanged, which suggests that the distance between Mn^{2+} ions in doped ISC-10-CdInS is too far to interact with each other. Such distribution of Mn^{2+} dopants is caused by the special coreless structure model with only one vacant site in each T5 nanocluster, which greatly limits the degree of doping concentration of Mn^{2+} and effectively avoids Mn−Mn interactions.

PL Dynamics. To gain further insight into the PL mechanism of undoped and Mn^{2+}-doped ISC-10-CdInS, it is essential to study their time-resolved PL dynamics. The time-correlated single photon-counting (TCSPC) experiments are performed, and all time-dependent PL curves are fitted to a multiexponential function $I(t) = \sum A_i \exp(-t/\tau_i)$. The average lifetimes are determined by the expression $\tau_{ave} = \sum A_i \tau_i^2 / \sum A_i \tau_i$.[80]

The PL dynamics for undoped sample at different emission positions (480, 550, 630, and 700 nm) at the room temperature is displayed in Figure 9a. All these PL decay curves can be fitted by triexponential decay curves. Their time constants (τ_1, τ_2, and τ_3) and normalized amplitudes of the components (A_1, A_2, and A_3) at $t = 0$ obtained by the fitting are summarized in Table S2 (Supporting Information). From this table, we notice that the two fast decay components for four different monitored emission positions are in the range of 1 to several tens of nanoseconds, which are typically derived from the nonradiative decay and surface trap (or defect) emission. Notably, the slow decay component with the time constants of several hundreds of nanoseconds is much greater than the former two fast components. This abnormal long lifetime may be caused by the coreless sites in the nanoclusters, which could be regarded as intrinsic deep trap (or defect) state and serve as new hole trap state for dominant deexciton process, since the deeper trap usually gives a longer lifetime than the shallow trap.[81] However, for the acid-washed ISC-10-CdInS, the average lifetimes for the same four emission positions drop back to the scale of 1 to several tens of nanoseconds (Figure 9b). The slow components for the acid-treated sample disappear. This is mainly because the pathway of excited electrons to deep intrinsic "defects" is drastically suppressed by the large amount of surface defects of microcrystals, which is easily created during the acid-washing step.

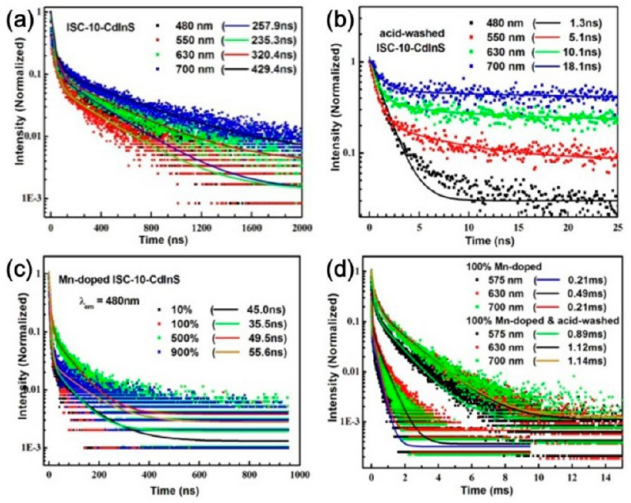

Figure 9. PL dynamics of emission at different emission center under interband excitation at 400 nm at room temperature: (a) raw ISC-10-CdInS, (b) acid-washed ISC-10-CdInS, (c) Mn^{2+}-doped sample with different doping level and monitored at 480 nm, and (d) 100% Mn^{2+}-doped and/or acid-washed sample monitored at 630 nm.

Mn^{2+} ion dopant in the T5 nanocluster markedly changes the PL dynamics of host matrix. As shown in Figure 9c and Table S3 (Supporting Information), the average lifetimes at 480 nm emission for various Mn^{2+}-doped samples are in the range of 35−55 ns, which indicates the deep defect-related emission with long lifetime is dramatically suppressed by the incorporated Mn^{2+} ions. In addition, we also notice that the kinetic decay time at the red emission band (575−700 nm) reached up to several hundreds of microseconds, similar to previously reported values for Mn^{2+}-doped II−VI semiconductor NCs (Figure 9d). These long decay times in the Mn^{2+}-doped nanocluster could be originated from the effective energy transfer process from excitons of T5 nanocluster to Mn^{2+} ions.[82] Spin and orbitally forbidden $^4T_1$ (spin 3/2) $\rightarrow {}^6A_1$ (spin 5/2) transition in Mn^{2+} ions results in a very long lifetime in the range of several hundreds of microseconds to several milliseconds. So, the replacement of intrinsic deep trap state by Mn^{2+} trap state could explain the short lifetime at 480 nm emission.

Normally, the lifetime of Mn^{2+} emission is reduced at higher concentrations in semiconductor NCs because of exchange interaction of coupled Mn^{2+} pairs partially lifting the spin selection rule.[72,83] However, in our case, the average lifetime of red emission at 630 nm is close to 0.5 ms, independent of Mn^{2+}-doping level (Table S4, Supporting Information). Unexpectedly, for 100% Mn^{2+}-doped and acid-washed sample with weak emission intensity caused by surface-trap states, the average lifetime at 630 nm reaches up to 1.1 ms, more than double that of unwashed sample. This enhanced lifetime is attributed to the absolute isolated distribution of Mn^{2+} ion in the nanocluster without any interference of Mn^{2+}-pairs attached on crystal.

Effect of Temperature on Mn^{2+}-Related PL Property. Temperature-dependent PL of Mn^{2+}-doped semiconductor can provide useful information on crystal field strength of dopant, energy transfer between excitons and dopants, and electron−

dx.doi.org/10.1021/ja501288x | J. Am. Chem. Soc. 2014, 136, 4769−4779

phonon coupling. Generally, the temperature quenching mainly results from the phonon-involved thermal dissociation of the excitons, which reduces the efficiency of the energy transfer from the exciton to Mn^{2+} ion. Compared with bulk crystal, NCs usually exhibit weak temperature quenching of PL due to hard dissociation of exciton in the confined space. In this work, we find that 5% Mn^{2+}-doped ISC-10-CdInS possesses a strong temperature quenching behavior for Mn^{2+} emission (Figure 10a), similar to the Mn^{2+}-doped ZnS bulk sample.[84] The

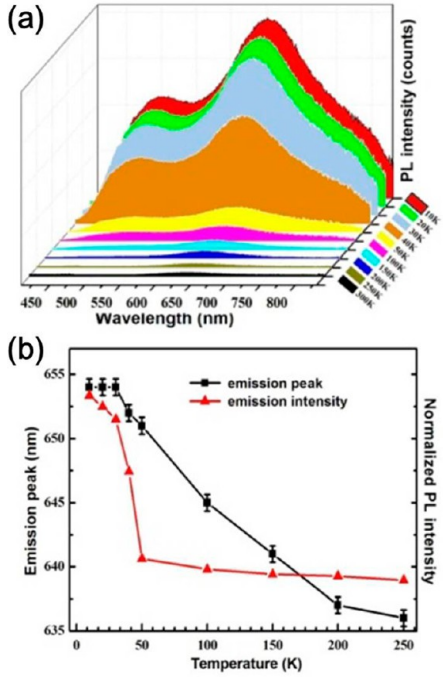

Figure 10. (a) Temperature dependence of emission spectra with interband excitation wavelength of 360 nm. (b) Temperature dependence of emission intensity at 630 nm and maximum peak wavelength for 5% Mn^{2+}-doped sample.

observation illustrates that this cluster-molecule-based micrometer-sized crystal still behaves like bulk sample, in which the photogenerated electron−hole pairs in the T5 nanocluster are easily dissociated because of exciton−phonon coupling. It is also very interesting that the peak wavelength of the Mn^{2+} emission shifts from 630 to 654 nm when the temperature decreases from room temperature to 30 K, as seen in Figure 10b. The red shift of the Mn^{2+} emission wavelength is also due to the enhancement of the crystal field strength caused by crystal lattice contraction at low temperature. With the decreasing temperature, the emitting state ($^4T_1$) of Mn^{2+} shifts to lower energy, and consequently shifts the emission to longer wavelength.[85]

EPR Signals. To further elucidate the local environment of Mn^{2+} ion in the crystal lattice of doped ISC-10-CdInS, we performed X-band electron spin resonance (ESR) spectroscopy study, which is an ultrasensitive probe to gain insight on sites having paramagnetic moments.[86] A distinctive feature of Mn^{2+} EPR signals is six-line hyperfine splitting, originating from the interaction between the spin ($S = 5/2$) of the unpaired 3d-electrons and spin ($I = 5/2$) of the ^{55}Mn nucleus. EPR spectra of undoped and doped solid samples are shown in Figure 11. For as-synthesized 100% Mn^{2+}-doped sample, there is a broad EPR signal. The broad background is most likely caused by a

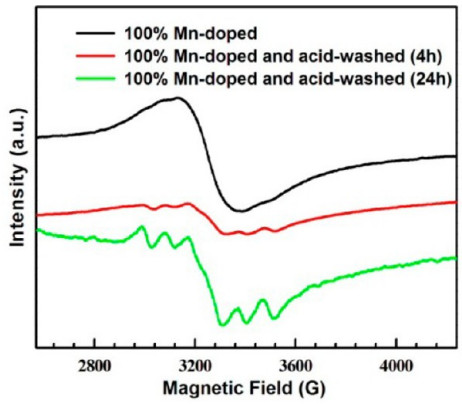

Figure 11. Electron paramagnetic resonance (EPR) spectroscopic characterization of Mn^{2+}-doped ISC-10-CdInS.

small amount of Mn^{2+}-pairs attached to the microcrystal surface upon doping process. The Mn−Mn interactions lead to a reduction of the electron−nuclear spin interactions in an individual Mn^{2+} ion.[87] To get rid of the interference from Mn^{2+}-pairs on the EPR test, we carefully wash this highly doped sample. When the sample is treated by diluted HCl acid for 4 h, some weak partially resolved peaks superimposed on a broad background signal are observed. As we expected, fully acid-washed sample exhibits an apparent six-line hyperfine splitting pattern, which is typical for isolated Mn^{2+} ions in the environment of host crystal. In fact, for the ideal mono-manganese doping case, the shortest Mn−Mn distance in the intercluster is around 15.29 Å, which is too far to form spin−spin interaction. The current results further provide solid evidence on well-dispersed dopant distribution without the formation of Mn^{2+} pairs in one supertetrahedral nanocluster through cation exchange.

Characterization of the Core Status in T5-ZnInS Nanocluster. We ever created a zinc-containing analogue of ISC-10-CdInS by replacing $Cd(Ac)_2$ with $Zn(Ac)_2$ during the preparation. This new compound (coded as ISC-10-ZnInS) exhibits a similar PXRD pattern with ISC-10-CdInS, indicating that it is also composed of T5 nanocluster (Figure S3, Supporting Information). Unfortunately, we cannot ascertain whether the core site in T5-ZnInS nanocluster is vacant or occupied by one Zn ion, since no good quality crystal is available for structure refinement. Inspired by above investigation on Mn^{2+}-related PL of ISC-10-CdInS, we realize that the characteristic red emission from dopant Mn^{2+} ion could be used as special feature to probe the defect status in this type of nanoclusters.

The replacement of Cd^{2+} by Zn^{2+} in T5 nanocluster blue shifts the band gap of ISC-10-ZnInS to 3.23 eV (Figure S4, Supporting Information). The enhanced energy gap leads to the corresponding blue shift of defect-related emission (~485 nm) from ISC-10-ZnInS host, compared with ISC-10-CdInS. Figure 12 displays the PL spectra of Mn^{2+}-doped ISC-10-ZnInS. It is clearly noticed that the red emission band appears and gradually suppresses the green emission with the increasing Mn^{2+}-doping level. This observation ambiguously proves the core site in T5-ZnInS nanocluster is still coreless. However, different from Mn^{2+}-doped ISC-10-CdInS, its maximum emission position is at 625 nm. This slight blue shift can be also explained by "crystal lattice strain" theory. The suppression degree of Mn−S bond in the "Mn@ZnS@InS core-shell"

dx.doi.org/10.1021/ja501288x | J. Am. Chem. Soc. 2014, 136, 4769−4779

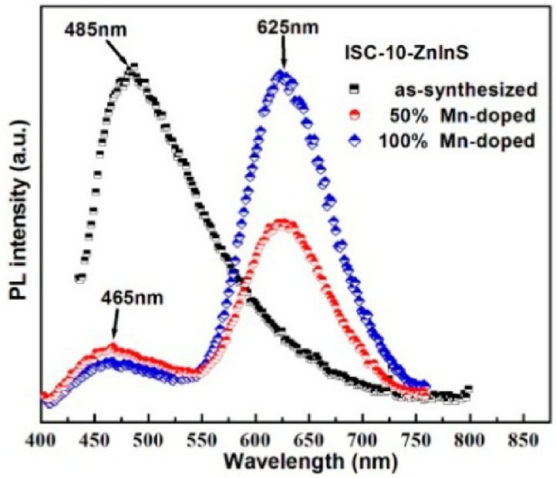

Figure 12. The PL spectra of ISC-10-ZnInS at room temperature.

nanocluster is smaller than that in "Mn@CdS@InS core-shell" because the size of the Zn^{2+} ion (0.74 Å) is considerably smaller than that of the Cd^{2+} ion (0.95 Å). In other words, there is more void space for Mn^{2+} ion in T5-ZnInS nanocluster. As a consequence, the crystal field splitting of Mn^{2+} d-orbitals in T5-ZnInS is smaller than that in T5-CdInS nanocluster and, in turn, leads to lifted $^4T_1$ level and the blue-shift of the PL peak position.[76]

PL Mechanism. On the basis of above results obtained, we can tentatively speculate on the complicated PL mechanism on the recombination process of photogenerated electron−hole pairs or excitons in the undoped and Mn^{2+}-doped microcrystals of ISC-10-CdInS. Figure 13 shows a schematic representation of the proposed mechanism for the PL excitation and energy transfer. Under interband irradiation, electron−hole pairs are generated in the energy levels of the T5-CdInS nanoclusters in undoped sample. The direct recombination of the electrons from the conduction band (CB) and holes from the valence band (VB) is usually named as the band edge emission (PL1).

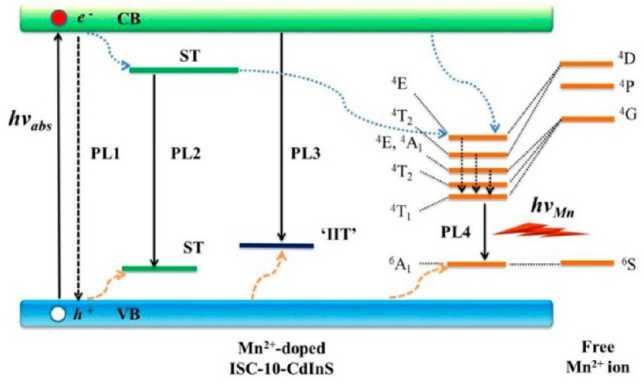

Figure 13. Schematic representation of the proposed mechanism for the PL excitation, the energy transfer and the PL emission in undoped and Mn^{2+}-doped ISC-10-CdInS. (The orange lines represent energy-level diagram of the Mn^{2+} ion in a free-ion state and tetrahedrally coordinated environment in supertetrahedral nanocluster. The solid arrows represent absorption and radiative transitions. Dotted arrows indicate nonradiative transitions. ST = surface trap. IIT = intrinsic internal trap. PL1, PL2, PL3, and PL4 represent different PL emission pathways: band emission, surface-trap-related emission, internal-trap-related emission, and Mn^{2+}-related emission, respectively.)

It is obviously that such band edge emission is substantially suppressed as a result of the missing of band emission in the range of 400 to 420 nm. However, the photogenerated electrons at CB and holes at VB are more easily transferred to the level of surface defects state, and the energy can be relaxed by PL2 pathway. In addition, a number of the holes in VB could be trapped by "intrinsic internal defects (IID)" at the core site of T5 nanocluster, where the excited electrons will be de-excited through PL3 pathway. Thus, the broadened green emission band is associated with the recombination of charge carriers or donor−acceptor pairs at surface defects of microcrystals with the lifetime of several tens of nanoseconds and at "IIDs" with the lifetime of several hundreds of nanoseconds.

It is generally accepted that the lowest excited state (^4G) for a free Mn^{2+} ion will split into four energy levels ($^4T_1$, $^4T_2$, ^4E and $^4A_1$) for the tetrahedrally coordinated Mn^{2+} ion according to the well-known Tanabe−Sugano diagrams.[68] These energy trap states in Mn^{2+} ions will replace the "IID" trap state when the Mn^{2+} ions are incorporated into the core site of T5 nanocluster. The excited electrons can be rapidly transferred to the $^4T_1$ state of the Mn^{2+} ion and decay radiatively to the $^6A_1$ state, giving a red emission through PL4 pathway. Therefore, several competition processes on the exciton dynamics will happen in this Mn^{2+}-doped sample. As previously observed, with the increasing doping level, more Mn^{2+} ions serve as trap centers to accept the photoexcited electron, which markedly makes the PL2/PL3 relaxation pathways suppressed and enhances the efficiency of Mn^{2+}-related emission. It should be noted that the PL4 relaxation pathway only occurs when the host matrix is excited under interband irradiation. There will be no excited electron transferring from CB to $^4T_1$ energy state if under intraband excitation. This is why the red emission gradually disappears and green emission shows up with the increasing excitation wavelength.

■ CONCLUSIONS

In summary, we have successfully realized atomically precise doping of Mn^{2+} ion into coreless supertetrahedral nanocluster with well-defined structure and uniform size through a two-step process involving presynthesis of crystalline clusters followed by diffusion doping. It is the special model structure with long-ranged ordered intrinsic vacancy in the supertetrahedral nanocluster that makes Mn^{2+} dopants disperse evenly and effectively avoids the formation of Mn-cluster in the nanocluster-based host matrix. Such atomically precise control is hard to be observed in traditional Mn^{2+}-doped II−VI semiconductors. This Mn^{2+}-doped material further serves as an ideal model for probing the PL property of Mn^{2+}-doped semiconductor microcrystal. The Mn^{2+} dopants dramatically change optical properties relative to the pristine host model. The Mn^{2+}-doped sample displays a strong red emission peak centered at 630 nm at room temperature (even bigger red shift to 654 nm at 30 K), which is clearly separated from the surface-defect/internal trap-state emissions with a maximum wavelength of ∼490 nm and is believed to arise from excition-Mn^{2+} energy transfer and subsequent dipole-forbidden $^4T_1$−$^6A_1$ ligand field transition. The big red shift relative to typical Mn^{2+} ion in II−VI semiconductor is the result of the local "crystal lattice strain" induced by the special supertetrahedral "Mn@CdS@InS core-shell" nanostructure with T_d symmetry. Such ordered distribution of Mn^{2+} dopants in semiconducting materials would likely enhance other properties such as

dx.doi.org/10.1021/ja501288x | J. Am. Chem. Soc. 2014, 136, 4769−4779

magneto-optical and electroluminescence as well, which will form the subject of future studies.

■ ASSOCIATED CONTENT

Supporting Information

Additional tables and figures. This material is available free of charge via the Internet at http://pubs.acs.org.

■ AUTHOR INFORMATION

Corresponding Author

wutao@suda.edu.cn; xianhui.bu@csulb.edu; pingyun.feng@ucr.edu

Notes

The authors declare no competing financial interest.

■ ACKNOWLEDGMENTS

This work was supported by National Natural Science Foundation of China (No. 21271135), a start-up fund (Q410900712) from Soochow University, the Priority Academic Program Development of Jiangsu Higher Education Institutions (PAPD), Young Thousand Talented Program, and the U.S. National Science Foundation (NSF) (P.F., DMR-1200451).

■ REFERENCES

(1) Kaib, T.; Haddadpour, S.; Andersen, H. F.; Mayrhofer, L.; Järvi, T. T.; Moseler, M.; Möller, K.-C.; Dehnen, S. *Adv. Funct. Mater.* **2013**, *23*, 5693.

(2) Bron, P.; Johansson, S.; Zick, K.; auf der Gunne, J. S.; Dehnen, S.; Roling, B. *J. Am. Chem. Soc.* **2013**, *135*, 15694.

(3) Shafaei-Fallah, M.; Rothenberger, A.; Katsoulidis, A. P.; He, J.; Malliakas, C. D.; Kanatzidis, M. G. *Adv. Mater.* **2011**, *23*, 4857.

(4) Ding, N.; Kanatzidis, M. G. *Nat. Chem.* **2010**, *2*, 187.

(5) Armatas, G. S.; Kanatzidis, M. G. *Nat. Mater.* **2009**, *8*, 217.

(6) Vaqueiro, P. *Dalton Trans.* **2010**, *39*, 5965.

(7) Vaqueiro, P.; Romero, M. L. *J. Am. Chem. Soc.* **2008**, *130*, 9630.

(8) Vaqueiro, P.; Romero, M. L. *Chem. Commun.* **2007**, 3282.

(9) Su, W. P.; Huang, X. Y.; Li, J.; Fu, H. X. *J. Am. Chem. Soc.* **2002**, *124*, 12944.

(10) Li, H. L.; Laine, A.; O'Keeffe, M.; Yaghi, O. M. *Science* **1999**, *283*, 1145.

(11) Gao, J. K.; Tay, Q. L.; Xiong, W.-W.; Li, P. Z.; Zhao, Y. L.; Chen, Z.; Zhang, Q. C. *Chem.—Asian J.* **2014**, *9*, 131.

(12) Xiong, W.-W.; Athersh, E. U.; Ng, Y. T.; Ding, J. F.; Wu, T.; Zhang, Q. C. *J. Am. Chem. Soc.* **2013**, *135*, 1256.

(13) Xiong, W.-W.; Li, P.-Z.; Zhou, T.-H.; Tok, A. I. Y.; Xu, R.; Zhao, Y. L.; Zhang, Q. C. *Inorg. Chem.* **2013**, *52*, 4148.

(14) Norris, D. J.; Efros, A. L.; Erwin, S. C. *Science* **2008**, *319*, 1776.

(15) Erwin, S. C.; Zu, L.; Haftel, M. I.; Efros, A. L.; Kennedy, T. A.; Norris, D. J. *Nature* **2005**, *436*, 91.

(16) Yang, H.; He, X.-W.; Wang, F.; Kang, Y.; Zhang, J. *J. Mater. Chem.* **2012**, *22*, 21849.

(17) Vinayan, B. P.; Nagar, R.; Rajalakshmi, N.; Ramaprabhu, S. *Adv. Funct. Mater.* **2012**, *22*, 3519.

(18) Long, Y. W.; Hayashi, N.; Saito, T.; Azuma, M.; Muranaka, S.; Shimakawa, Y. *Nature* **2009**, *458*, 60.

(19) Pradhan, N.; Peng, X. *J. Am. Chem. Soc.* **2007**, *129*, 3339.

(20) Wang, C.; Xie, Z.; deKrafft, K. E.; Lin, W. *J. Am. Chem. Soc.* **2011**, *133*, 13445.

(21) He, J.; Zhao, L.-D.; Zheng, J.-C.; Doak, J. W.; Wu, H.; Wang, H.-Q.; Lee, Y.; Wolverton, C.; Kanatzidis, M. G.; Dravid, V. P. *J. Am. Chem. Soc.* **2013**, *135*, 4624.

(22) He, J. Q.; Androulakis, J.; Kanatzidis, M. G.; Dravid, V. P. *Nano Lett.* **2012**, *12*, 343.

(23) He, J.; Blum, I. D.; Wang, H.-Q.; Girard, S. N.; Doak, J.; Zhao, L.-D.; Zheng, J.-C.; Casillas, G.; Wolverton, C.; Jose-Yacaman, M.; Seidman, D. N.; Kanatzidis, M. G.; Dravid, V. P. *Nano Lett.* **2012**, *12*, 5979.

(24) Tantang, H. S.; Xiao, J. C.; Wei, J.; Chan-Park, M. B. E.; Li, L. J.; Zhang, Q. C. *Eur. J. Inorg. Chem.* **2011**, 4182.

(25) Qian, H.; Jiang, D.-e.; Li, G.; Gayathri, C.; Das, A.; Gil, R. R.; Jin, R. *J. Am. Chem. Soc.* **2012**, *134*, 16159.

(26) Wang, L.-M.; Bulusu, S.; Huang, W.; Pal, R.; Wang, L.-S.; Zeng, X. C. *J. Am. Chem. Soc.* **2007**, *129*, 15136.

(27) Yamada, M.; Akasaka, T.; Nagase, S. *Acc. Chem. Res.* **2009**, *43*, 92.

(28) Lips, F.; Clerac, R.; Dehnen, S. *Angew. Chem., Int. Ed.* **2011**, *50*, 960.

(29) Lips, F.; Holynska, M.; Clerac, R.; Linne, U.; Schellenberg, I.; Pottgen, R.; Weigend, F.; Dehnen, S. *J. Am. Chem. Soc.* **2012**, *134*, 1181.

(30) Deng, Z. T.; Tong, L.; Flores, M.; Lin, S.; Cheng, J. X.; Yan, H.; Liu, Y. *J. Am. Chem. Soc.* **2011**, *133*, 5389.

(31) Samokhvalov, P.; Artemyev, M.; Nabiev, I. *Chem.—Eur. J.* **2013**, *19*, 1534.

(32) Srivastava, B. B.; Jana, S.; Pradhan, N. *J. Am. Chem. Soc.* **2010**, *133*, 1007.

(33) Girard, S. N.; He, J.; Zhou, X.; Shoemaker, D.; Jaworski, C. M.; Uher, C.; Dravid, V. P.; Heremans, J. P.; Kanatzidis, M. G. *J. Am. Chem. Soc.* **2011**, *133*, 16588.

(34) Mocatta, D.; Cohen, G.; Schattner, J.; Millo, O.; Rabani, E.; Banin, U. *Science* **2011**, *332*, 77.

(35) Zhang, W.; Zhou, X.; Zhong, X. *Inorg. Chem.* **2012**, *51*, 3579.

(36) Deng, D.; Cao, J.; Qu, L.; Achilefu, S.; Gu, Y. *Phys. Chem. Chem. Phys.* **2013**, *15*, 5078.

(37) Jana, S.; Srivastava, B. B.; Jana, S.; Bose, R.; Pradhan, N. *J. Phys. Chem. Lett.* **2012**, *3*, 2535.

(38) Bhargava, R. N.; Gallagher, D.; Hong, X.; Nurmikko, A. *Phys. Rev. Lett.* **1994**, *72*, 416.

(39) Xiong, W. *J. Phys. D: Appl. Phys.* **2012**, *45*, 345101.

(40) Viswanatha, R.; Pietryga, J. M.; Klimov, V. I.; Crooker, S. A. *Phys. Rev. Lett.* **2011**, *107*, 067402.

(41) Furdyna, J. K. *J. Appl. Phys.* **1988**, *64*, R29.

(42) Zhao, H.-Y.; Zhao, J.-W.; Yang, B.-F.; He, H.; Yang, G.-Y. *Cryst. Growth Des.* **2013**, *13*, 5169.

(43) Zheng, S.-T.; Yang, G.-Y. *Chem. Soc. Rev.* **2012**, *41*, 7623.

(44) Hołyńska, M.; Frank, N.; Pichon, C.; Jeon, I.-R.; Clérac, R.; Dehnen, S. *Inorg. Chem.* **2013**, *52*, 7317.

(45) Wu, P.; Miao, L.-N.; Wang, H.-F.; Shao, X.-G.; Yan, X.-P. *Angew. Chem., Int. Ed.* **2011**, *50*, 8118.

(46) Panda, S. K.; Hickey, S. G.; Demir, H. V.; Eychmüller, A. *Angew. Chem., Int. Ed.* **2011**, *50*, 4432.

(47) Santra, P. K.; Kamat, P. V. *J. Am. Chem. Soc.* **2012**, *134*, 2508.

(48) Luo, J. H.; Wei, H. Y.; Huang, Q. L.; Hu, X.; Zhao, H. F.; Yu, R. C.; Li, D. M.; Luo, Y. H.; Meng, Q. B. *Chem. Commun.* **2013**, *49*, 3881.

(49) Le Donne, A.; Jana, S. K.; Banerjee, S.; Basu, S.; Binetti, S. *J. Appl. Phys.* **2013**, *113*, 014903.

(50) Beaulac, R.; Archer, P. I.; Ochsenbein, S. T.; Gamelin, D. R. *Adv. Funct. Mater.* **2008**, *18*, 3873.

(51) Wu, P.; Yan, X.-P. *Chem. Soc. Rev.* **2013**, *42*, 5489.

(52) Maity, A. R.; Palmal, S.; Basiruddin, S. K.; Karan, N. S.; Sarkar, S.; Pradhan, N.; Jana, N. R. *Nanoscale* **2013**, *5*, 5506.

(53) Geszke-Moritz, M.; Piotrowska, H.; Murias, M.; Balan, L.; Moritz, M.; Lulek, J.; Schneider, R. *J. Mater. Chem. B* **2013**, *1*, 698.

(54) Galicka, M.; Buczko, R.; Kacman, P. *Nano Lett.* **2011**, *11*, 3319.

(55) Manna, G.; Jana, S.; Bose, R.; Pradhan, N. *J. Phys. Chem. Lett.* **2012**, *3*, 2528.

(56) Aldakov, D.; Lefrancois, A.; Reiss, P. *J. Mater. Chem.C* **2013**, *1*, 3756.

(57) Eilers, J.; Groeneveld, E.; de Mello Donegá, C.; Meijerink, A. *J. Phys. Chem. Lett.* **2012**, *3*, 1663.

(58) Nag, A.; Cherian, R.; Mahadevan, P.; Gopal, A. V.; Hazarika, A.; Mohan, A.; Vengurlekar, A. S.; Sarma, D. D. *J. Phys. Chem. C* **2010**, *114*, 18323.

(59) Tanaka, M.; Qi, J.; Masumoto, Y. *J. Cryst. Growth* **2000**, *214/215*, 410.
(60) Gao, X. H.; Cui, Y. Y.; Levenson, R. M.; Chung, L. W. K.; Nie, S. M. *Nat. Biotechnol.* **2004**, *22*, 969.
(61) Manzoor, K.; Johny, S.; Thomas, D.; Setua, S.; Menon, D.; Nair, S. *Nanotechnology* **2009**, *20*, 065102.
(62) Chen, H.-Y.; Maiti, S.; Son, D. H. *ACS Nano* **2011**, *6*, 583.
(63) Yang, Y. A.; Chen, O.; Angerhofer, A.; Cao, Y. C. *J. Am. Chem. Soc.* **2006**, *128*, 12428.
(64) Pradhan, N.; Goorskey, D.; Thessing, J.; Peng, X. *J. Am. Chem. Soc.* **2005**, *127*, 17586.
(65) Yang, Y. A.; Chen, O.; Angerhofer, A.; Cao, Y. C. *Chem.—Eur. J.* **2009**, *15*, 3186.
(66) Wu, T.; Zhang, Q.; Hou, Y.; Wang, L.; Mao, C. Y.; Zheng, S. T.; Bu, X. H.; Feng, P. Y. *J. Am. Chem. Soc.* **2013**, *135*, 10250.
(67) Hoa, T. T. Q.; The, N. D.; McVitie, S.; Nam, N. H.; Vu, L. V.; Canh, T. D.; Long, N. N. *Opt. Mater.* **2011**, *33*, 308.
(68) Tanaka, M.; Qi, J.; Masumoto, Y. *J. Lumin.* **2000**, *87−89*, 472.
(69) Counio, G.; Gacoin, T.; Boilot, J. P. *J. Phys. Chem. B* **1998**, *102*, 5257.
(70) Yoon, K. H.; Ahn, J. K.; Cho, J. Y. *J. Mater. Sci.* **2001**, *36*, 1373.
(71) Ramasamy, P.; Mamum, S. I.; Jang, J.; Kim, J. *CrystEngComm* **2013**, *15*, 2061.
(72) Jindal, Z.; Verma, N. K. *J. Mater. Sci.* **2008**, *43*, 6539.
(73) Xu, H.; Zhang, W.; Jin, W.; Ding, Y.; Zhong, X. *J. Lumin.* **2013**, *135*, 47.
(74) Torimoto, T.; Adachi, T.; Okazaki, K.-i.; Sakuraoka, M.; Shibayama, T.; Ohtani, B.; Kudo, A.; Kuwabata, S. *J. Am. Chem. Soc.* **2007**, *129*, 12388.
(75) Wang, C.; Li, Y. Q.; Bu, X. H.; Zheng, N. F.; Zivkovic, O.; Yang, C. S.; Feng, P. Y. *J. Am. Chem. Soc.* **2001**, *123*, 11506.
(76) Cao, S.; Zheng, J.; Zhao, J.; Wang, L.; Gao, F.; Wei, G.; Zeng, R.; Tian, L.; Yang, W. *J. Mater. Chem. C* **2013**, *1*, 2540.
(77) Zuo, T.; Sun, Z.; Zhao, Y.; Jiang, X.; Gao, X. *J. Am. Chem. Soc.* **2010**, *132*, 6618.
(78) Yang, H. S.; Holloway, P. H.; Ratna, B. B. *J. Appl. Phys.* **2003**, *93*, 586.
(79) Zhou, W. C.; Tang, D. S.; Zou, B. S. *Physica E-Low-Dimensional Systems & Nanostructures* **2013**, *47*, 162.
(80) Zhang, Y.; Jing, P.; Zeng, Q.; Sun, Y.; Su, H.; Wang, Y. A.; Kong, X.; Zhao, J.; Zhang, H. *J. Phys. Chem. C* **2009**, *113*, 1886.
(81) Karan, S.; Majumder, M.; Mallik, B. *Photochem. Photobiol. Sci.* **2012**, *11*, 1220.
(82) Kim, D.; Miyamoto, M.; Nakayama, M. *J. Appl. Phys.* **2006**, *100*, 094313.
(83) Suyver, J. F.; Wuister, S. F.; Kelly, J. J.; Meijerink, A. *Phys. Chem. Chem. Phys.* **2000**, *2*, 5445.
(84) Tanaka, M.; Masumoto, Y. *Chem. Phys. Lett.* **2000**, *324*, 249.
(85) Chen, W.; Su, F. H.; Li, G. H.; Joly, A. G.; Malm, J. O.; Bovin, J. O. *J. Appl. Phys.* **2002**, *92*, 1950.
(86) Gonzalez Beermann, P. A.; McGarvey, B. R.; Muralidharan, S.; Sung, R. C. W. *Chem. Mater.* **2004**, *16*, 915.
(87) Chin, P. T. K.; Stouwdam, J. W.; Janssen, R. A. J. *Nano Lett.* **2009**, *9*, 745.